Increasing the Traditional Child-Langmuir Limited Current Density in Ion Thrusters through Plasma Potential Modification

IEPC-2015-381／ISTS-2015-b-381

Presented at Joint Conference of 30th International Symposium on Space Technology and Science, 34th International Electric Propulsion Conference and 6th Nano-satellite Symposium
Hyogo-Kobe, Japan
July 4–10, 2015

Neil A. Arthur* and John E. Foster†
University of Michigan, Ann Arbor, MI, 48104, USA

Abstract: The extractable beam current of gridded ion thrusters is space charge limited according to the Child-Langmuir law. This classic law does not consider the ion injection velocity into the grid sheath. This work shows that when the ions are injected into the grid plane with an appreciable velocity, the extractable beam current increases. The ion drift velocity is created by modifying the plasma potential, which is accomplished through biasing the individual magnet rings in a four ring, magnetic cusp ion thruster. When the plasma potential downstream of the grid is increased, the ions see a larger potential drop and are accelerated towards the grid. The increase in ion drift velocity and plasma potential are demonstrated through the use of Mach probes. The increased ion current to the grid plane is verified by measuring the current of the collector grid. Finally, a retarding potential analyzer shows that the ion energy distribution function is shifted to higher energies, indicating an increased ion drift velocity.

*PhD Candidate, Nuclear Engineering and Radiological Sciences, arthurne@umich.edu
†Associate Professor, Nuclear Engineering and Radiological Sciences, jefoster@umich.edu

Nomenclature

A_{eff} = effective electrode area
A_{RPA} = RPA entrance surface area
$\vec{B}$ = magnetic field
c_s = ion sound speed
d = electrode gap
e = elementary charge
I_{beam} = ion beam current
I_C = RPA ion collector current
I_d = discharge current
I_{flow} = mass flow rate in equivalent amps
$I_{i,down}$ = downstream ion saturation current
$I_{i,up}$ = upstream ion saturation current
I_{sat} = measured electrode electron saturation current
J_{CL} = classical Child-Langmuir current density
J_{GCL} = generalized Child-Langmuir current density
l_w = leak width
$l_{w,i}$ = leak width for ions
$IEDF$ = ion energy distribution function
k = Boltzmann constant
$LCIF$ = laser collisional induced fluorescence
M = Mach number
m_e = electron mass
M_i = ion mass
n_e = electron density
N_g = neutral gas density
n_i = ion density
OAF = grid open area fraction
r_{mre} = manget ring electrode radius
r_{le} = electron Larmor radius
r_{li} = ion Larmor radius
RPA = retarding potential analyzer
T_e = electron temperature
V = electrode voltage
V_d = discharge voltage
V_D = RPA discriminator voltage
v_i = ion drift velocity
V_p = plasma potential
V_{sat} = saturation voltage
$v_\perp$ = velocity perpendicular to $\vec{B}$
β = Hall parameter
ϵ_0 = vacuum permittivity
$\vec{\phi}$ = electron flux
$\hat{\phi}_i$ = grid transparency to ions without beam extraction
ϕ_i = grid transparency to ions with beam extraction
η_d = discharge losses
η_p = propellant utilization efficiency
κ = Mach number proportionality constant
ν_m = momentum transfer collision frequency
σ_m = momentum transfer cross-section
Ω_e = electron cyclotron frequency

I. Introduction

Gridded ion thruster technology can potentially satisfy propulsion requirements for a range of different mission types. In recent times, gridded ion thrusters have largely been considered a high specific impulse, low thrust density system that is best suited for aggressive interplanetary missions or station keeping operations where time to a given delta-v is not as important. In this case, the appeal of gridded ion thrusters is remarkable increased payload fraction capacity relative to other options. Though this characterization is not accurate, the low thrust density misconception persists. In reality, though ion thrusters are space charge limited devices, actual operating beam current density, and thus thrust density, over the years has been reduced to increase overall engine lifetime. This low thrust density has also been artificially constrained by power limitations of the spacecraft, thus limiting the beam current at a given beam voltage. This de-rating is not desirable for those missions requiring high thrust and maneuvers of short duration.[1] For example, engines such as NEXT and NSTAR operate nominally at current densities below 5 mA/cm^2.[2] Ion engines however have been performance characterized at current densities well above the current de-rating limit imposed today. Thrust and thus thrust density of an ion engine can be increased by simply increasing the beam current. At a given total voltage, the upper limit of the current is limited by the Child-Langmuir law. Currently ion thrusters operate at only ∼40% of this limit, which translates into substatial growth potential.[3] Indeed, high thrust ion engines operating near the Child-Langmuir limit have been demonstrated in the past with thrust densities of 9 N/m^2.[4] The conventional Child-Langmuir law is not immutable. Operating beyond the conventional Child-Langmuir (CL) limit would allow for even larger growth potential, essentially enabling a high power, high thrust capability for the gridded ion technology. Conventionally, the CL limit sets the maximum current density at a given voltage as:

$$J_{CL} = \frac{4}{9}\epsilon_0 \sqrt{\frac{2e}{M_i}} \frac{V^{3/2}}{d^2} \tag{1}$$

where ϵ_0 is the vacuum permittivity, e is the elementary charge, M_i is the ion mass, V is the extraction voltage, and d is the grid gap distance. High beam current extraction can be achieved therefore only by significantly reducing the inter-electrode spacing, modifying the screen grid thickness or by operating at a higher total voltage. All such implementations are problematic in that they are limited by the hold off field limit of the grid set. This limit is approximately 3-4 kV/mm (graphite), above which arcing and associated erosion can occur, thus limiting life and stable operation. One way around the problem is to increase the size of the ion optics, while maintaining a small as practically operational gap. Beyond grid diameters of 50 cm however, it is difficult to maintain large span-to-gap ratios. Indeed, the annular ion engine concept addresses this aspect of scale up. Even the annular engine must grow to accommodate larger beam currents. Therefore, it should be pointed out that to minimize size to mass ratio for an engine with presumably enhanced performance capability (e.g. high power, high thrust to power, high thrust density), a new paradigm must be considered.

II. Theory

Because the beam current is proportional to the discharge current, if one is able to circumvent the space charge limited flow problem, then one is only limited by the capacity of the ionizer. Unfortunately, before one reaches the space charge limit, it is often the case that the ionizer is source limited. Source limitation is related to the ability to raise the plasma density. Plasma density tends to increase with increasing discharge current. It is known that multipole sources such as ring cusp engines go unstable when forced to operate above a threshold discharge current.[5] These instabilities are necessary in order to transport the additional electronic current through the magnetic cusps to the anode. The annular ion engine concept has the capacity to operate at discharge currents well above that of a conventional ring cusp engine.[3] This super-threshold operation is possible in the annular ion engine geometry owing to the introduction of additional electron collection surface area located on a cylindrically located stalk. Indeed, it is this stalk that gives the engine its annular appearance as it precludes ion extraction on centerline. In this respect, the use of an annular engine type solution will likely be required in order to realize operation near the space charge limit.

The conventional CL limit, shown in Eq. (1), is derived assuming the ion injection velocity is small compared to the grid accelerating total voltage. In this case, it is taken as zero. It turns out that if one includes a finite injection velocity, it is still possible to obtain an analytical expression of the current. This current increases with injection velocity and is thus a means to increase beam current. The generalized Child-Langmuir current density becomes[6]

$$J_{GCL} = J_{CL} \left(1 + \frac{M_i v_i^2}{2eV}\right)^{3/2} \tag{2}$$

where v_i is the ion velocity. In general, added directed ion drift will increase ion flow to the extraction plane, regardless of how near or far one is to the conventional space charge limit. In this respect, adding ion drift is a means to increase beam current at a given operation condition, thus minimizing discharge losses. Figure 1 shows the increase in space charge limited current as a function velocity. It is possible to approach a 2x increase by increasing the drift velocity to several thousand m/s. Increasing the ion drift velocity beyond 10^4 m/s is not practical as it would lead to grid erosion. Perhaps the most straightforward way to increase ion drift is to enhance the electric field directed towards the extraction plane. In this work we investigate a method to enhance this field by modifying the bulk plasma potential.

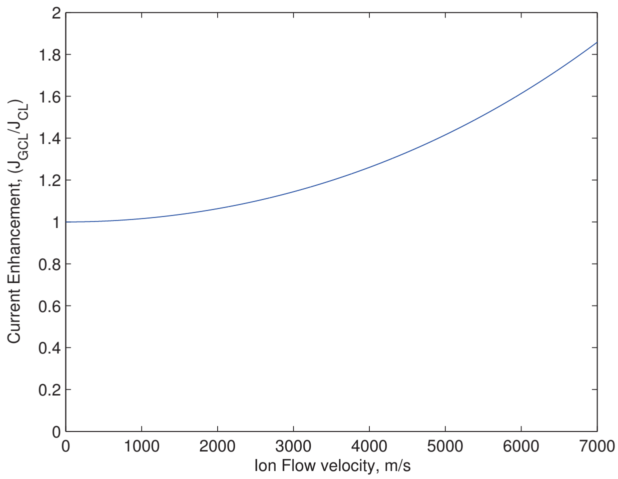

Figure 1: Child-Langmuir current density enhancement as a function of ion drift velocity.

A. Approach to Modifying the Plasma Potential

In general, the bulk plasma potential is established by the relative loss rates of ions and the electrons, ultimately assuming a value that maintains quasineutrality. Affecting this loss rate in principle can affect the plasma potential. In ring cusp sources, the magnetic cusps are large scale structures that fan out into the bulk plasma and essentially facilitate electron collection to the anode. Because these structures are anchored to the magnet poles located at the anode surface, affecting the potential or potential distribution of a cusp should give rise to measurable changes in electron loss rates. Such changes in electron loss rates invariably should impact the bulk plasma potential. In this work, the potential of the collector rings at each magnetic cusp is varied and the response of the bulk plasma potential is measured. The distribution of electrons in magnetic cusps has been previously measured using laser collisional-induced fluorescence (LCIF).[7] Figure 2 depicts the electron distribution in and above the magnetic cusp. As can be seen here, the spatial extent of the magnetic cusp into the bulk is significant. By independently biasing the magnet rings, we aim to control the local plasma potential. In this work, rings 1-3 are biased, with biased potentials denoted as $V_{p,1}, V_{p,2},$ and $V_{p,3}$. Modifying the plasma potential can produce ion drifts within the device. With increased ion drift, not only is the ion flux available to be extracted increased, but also the upper space charge limited current magnitude is increased.

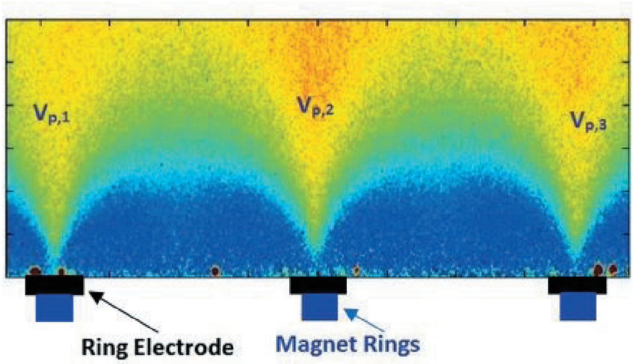

Figure 2: Magnetic cusps with ring electrodes biased to produce a modified plasma potential.

III. Experimental Setup

By raising the bulk plasma potential above the grid boundary potential, an enhanced drift field can be established. The potential drop across the magnetic cusps will change as well. The objective of this effort is to enhance ion flow to the grid plane at a given operating condition without appreciably affecting electron flow through the cusps. In this work, the plasma potential modification experiments take place with a 15 cm diameter, cylindrical ion source. This source has been used previously to study magnetic cusp physics.[8] The engine features four magnet rings, each of which are covered with a conformal, electrically isolated collection ring. These rings allow for the current distribution to measured at each cusp. In this investigation, the rings are also independently biased. A picture of this device and a schematic showing the isolated magnet ring electrodes can be seen in Figs. 3 and 4.

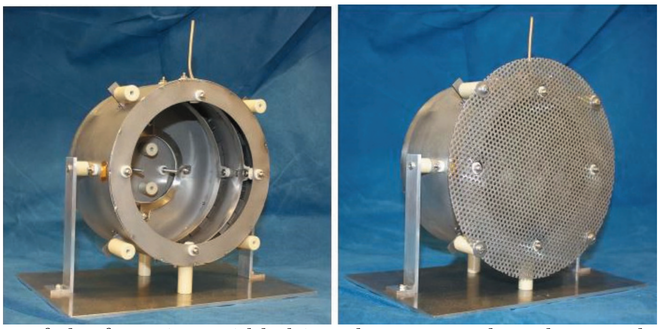
Figure 3: A picture of the four ring gridded ion thruster used as the test device for this work.

The electrical circuit diagram is shown in Fig. 5. In this diagram, magnet rings 1-3 and the anode shell are all at the same potential, while magnet ring 4 is biased independently. The anode was grounded. In this investigation, each magnet ring and shell was separately isolated and biased from -55 V to 25 V to acquire a current-voltage (IV) characteristic. The bias sweep was over a voltage range that did not appreciably affect the operating discharge voltage. Shunt resistors ($<10\text{m}\Omega$) were used to measure the current to each magnet ring, the shell, and the grid. A shunt resistor was also used to measure the current that passed through the magnet rings and shell on the way to ground as a check that the discharge current stayed constant while one of the magnet rings was biased.

A. Ion Drift Velocity

Qualitative measurements of ion flow were made using two Mach probes. A Mach probe is a double Langmuir probe with planar faces that are parallel to each other and electrically isolated. The difference in the ion current measured by each planar face can be used to infer ion drift. In general, Mach probes require anisotropic flow such as that realized in an ion beam or along a flux tube. In such a case, Mach probes

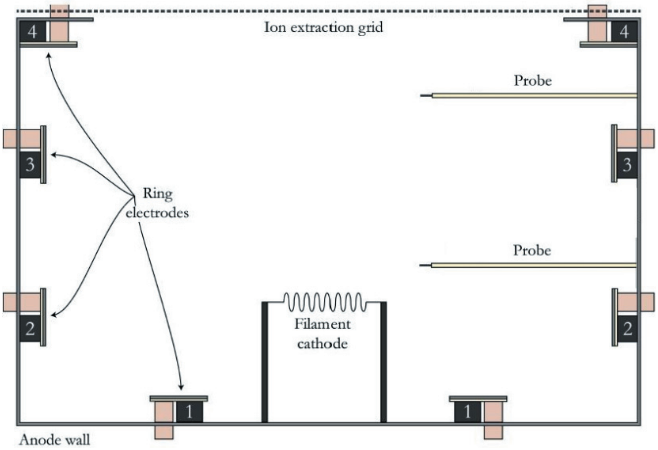

Figure 4: Discharge schematic showing the isolated magnet ring electrodes, the two probes, and the filament cathode.

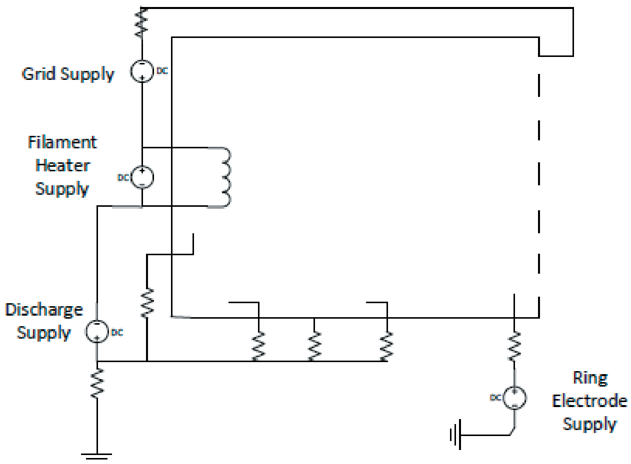

Figure 5: Electrical schematic showing magnet ring electrode 4 being biased relative to the other three rings and the shell.

measure the Mach number of the ions, given by:

$$M = \frac{v_i}{c_s} \tag{3}$$

and the sound speed, c_s, is given by

$$c_s = \sqrt{\frac{T_e}{M_i}} \tag{4}$$

where T_e is the electron temperature. The Mach number can be calculated from the ratio of ion saturation currents of the two probe faces according to the equation

$$M = \frac{1}{\kappa} \ln \frac{I_{i,up}}{I_{i,down}} \tag{5}$$

where κ is a constant that is dependent on T_e and the ion temperature, T_i. The ion saturation currents, $I_{i,up}$ and $I_{i,down}$ are measured by the upstream and downstream probe faces respectively. Previous studies have suggested that for $\frac{T_i}{T_e} \leq 3$, κ can be assumed to be 1.34 to within 10%.[9] As the ratio $\frac{T_i}{T_e}$ decreases, κ increases and for $\kappa \approx 2$, Eq. (5) can be approximated as[10]

$$M = \frac{I_{i,up} - I_{i,down}}{I_{i,up} + I_{i,down}} \tag{6}$$

This approximation is valid for $\frac{T_i}{T_e} \leq 1$. This condition is not valid in the ion beam produced by the thruster, but can be used within the bulk plasma inside the thruster discharge chamber.

The discharge performance is measured using two parameters: discharge losses and propellant utilization efficiency. The discharge losses are measured in W/A, according to the formula

$$\eta_d = \frac{V_d I_d}{I_{beam}} \tag{7}$$

where V_d and I_d are the discharge voltage and current respectively. The beam current, I_{beam}, must be corrected for when operating the thruster with simulated beam extraction using the formula[11]

$$I_{beam} = \frac{\phi_i I_{grid}}{1 - OAF} \tag{8}$$

where I_{grid} is the current collected by the grid, OAF is the open area fraction of the grid, and ϕ_i is the effective transparency of the grid to ions during beam extraction, which has been experimentally determined to be around 0.8.[11] The propellant utilization efficiency can be calculated as[11]

$$\eta_p = \frac{I_{beam}}{I_{flow} + I_{beam}\left(1 - \phi_i/\hat{\phi}_i\right)} \tag{9}$$

where $\hat{\phi}_i$ is the transparency of the gird to ions without beam extraction, experimentally measured to be 0.22.[11] Before plasma potential modification experiments were carried out, the discharge performance was optimized using simulated beam extraction methods.[11]

The ion source utilized a tungsten filament electron emitter. In this investigation, argon gas was used as the feed gas. Argon gas flows ranged from 20-30 sccm. During experiments, chamber pressure did not exceed 9×10^{-4} Torr. Experiments were conducted in a cylindrical vacuum chamber, 0.5 m in diameter by 2 m long. This chamber is capable of base pressures of 10^{-6} Torr.

In general, over the range investigated, discharge voltages varied between 30-50 V and discharge currents varied between 1-5 A. Discharge losses (η_d) were kept under 200 W/A for conditions investigated herein. The propellant utilization efficiency (η_p) was around 0.55, which is somewhat low. The low utilization is a consequence of operation with the filament and operation on argon as opposed to xenon. Interestingly, the utilization is highly sensitive to ring current and bias voltage, suggesting that by actively varying the current distribution, one may be able to impact engine efficiency.

IV. Experimental Results

The first step in this investigation was to map out reasonable operating conditions (η_d<200 W/A). Representative current distributions in this regime are shown in Fig. 6. Here the current distribution for a number of discharge currents are shown. As can be seen here, the current allotment to the magnet rings is similar with the anode shell collecting individually more than any of the magnet ring electrodes. Nonetheless, some 70% of the discharge current is carried via the magnet rings. The electrode above each magnet ring was independently biased from -55 V to 25 V in order to determine the plasma response. Additionally, the shell was biased over this range while the four magnet ring electrodes were shorted together. Over the voltage sweep, the current to each electrode was measured. As the voltage to a single magnet ring electrode was increased to a large positive value (>10 V), that magnet ring electrode became the dominant current collector, regardless of magnet ring position or discharge conditions. This suggests that a single magnet ring, and its associated cusp structure, can affect the entire bulk plasma.

A. Magnet Ring Electrode IV Responses to Independent Bias

Biasing a magnet ring measures the magnetized plasma response to the electric field changes at the electrode. The current collected at these electrodes reflects the plasma diffusion in the presence of a cusp magnetic field. Two Mach probes measure the bulk plasma properties and the drift velocity of ions in the plasma. Magnet ring electrode IV traces are shown in Fig. 8.

Biasing the rings allows one to assess the current capacity at a given ring. As can been seen in Fig. 8, the ring current IV characteristic has the form of a Langmuir probe trace. The curves show that one can collect

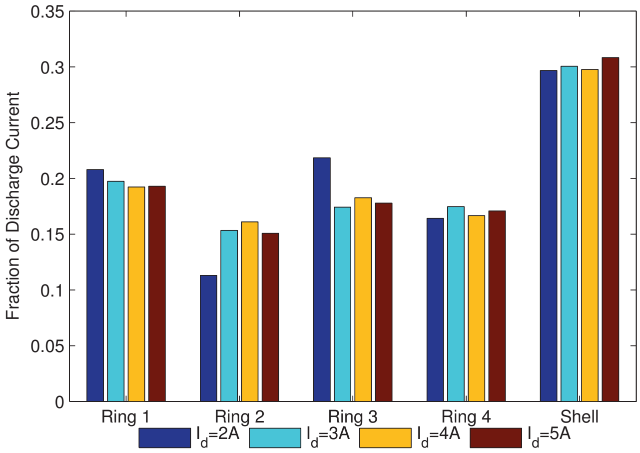

Figure 6: The current distribution to each magnet ring electrode and the shell for various discharge currents.

nearly the entire discharge current, at least over this range, by biasing a single ring. The maximum current collected at a given ring was always slightly less than the total discharge current—the remaining current collected at the other three rings and the anode shell. This can be seen in Fig. 7. At negative magnet ring electrode voltages, the discharge voltage remained constant; however, as the electrode voltage was increased positively, the discharge voltage fell slightly. The discharge voltage did not fall by the same amount as the magnet ring electrode voltage increased. As a magnet ring was biased from 0-25 V, the discharge voltage would fall by 1-10 V.

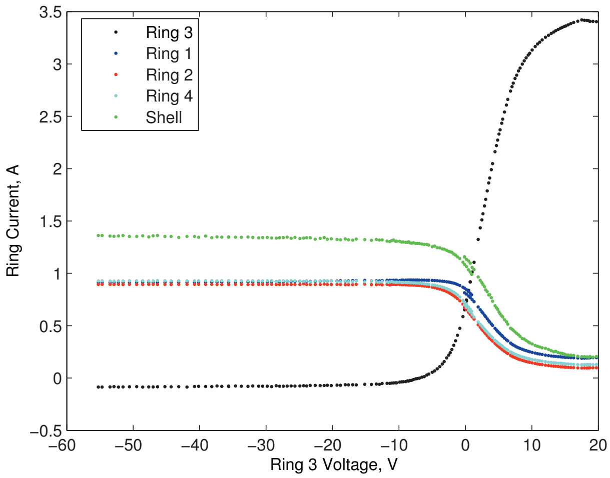

Figure 7: Current to all electrodes as a function of magnet ring electrode 3 voltage.

The data in Fig. 8 suggest that simply by biasing the rings, one can artificially specify the current distribution and thus directly specify the spatial plasma production profile for a given magnetic circuit. In this regard, it may be possible that, for a given thruster, one can actually optimize performance on the fly. The curves also indicate the ion current to the cusps. Typically, the bulk plasma potential is higher than the wall potential leading to ion flow to the wall. This flow is difficult to measure in practice because electrostatic probes do not work well in magnetic sheaths. Here we present actual measurements of ion current to the wall. This represents ion losses at the cusps. The“retarding” region connecting the electron and ion saturation region is also pronounced in the figures as well. This retarding region is a measure of the voltage changes required to realize large changes in collected electron current through the sheath. In this case, we observe the bulk electron response to the applied field across the magnetosheath. Here, the slope of this region is a measure of electron transport across and along cusp field lines under the influence of an electric field. Because the magnetic field does not do work on the electrons however, the “retarding” region can be expected to yield insight into the energetics of electrons reaching the ring electrode. The slope is therefore a measure of the effective electron temperature of electrons that make it through the cusp. In this regard, it gives some insight into the nature of the plasma at the magnetic cusp boundary. The knee of the curves is associated with the potential that gives rise to the collection of nearly all the discharge electron current. One can assume that this potential is associated with maximum drain of electron flux tubes. This voltage is not directly relatable to the actual plasma potential however because electron flux across the magnetosheath can be enhanced by the applied field. Biasing the ring at actual bulk plasma potential would give rise to zero electric field in the sheath and thus electrons reaching the surface would do so because of diffusion alone. The knee is therefore designated as a saturation potential.

B. Electron Mobility in $\vec{E}$ and $\vec{B}$ Fields

From a theoretical standpoint, electron transport through the cusps can be modeled. The electron mobility and diffusion coefficients are both a function of electron temperature, in the case of both a magnetic and electric field, the electron flux equation is

$$\vec{\phi} = en_e\overline{\overline{\mu}}(T_e) \cdot \vec{E} - \overline{\overline{D}}(T_e) \cdot \nabla n_e \tag{10}$$

where n_e is the electron density. The mobility, $\overline{\overline{\mu}}(T_e)$, and diffusion, $\overline{\overline{D}}(T_e)$, coefficients are both tensors. Equation (10) accounts for electron flux along flux tubes, which are parallel to the $\vec{B}$ field lines, as well as the flux due to cross field diffusion via collisions. The equation of motion for electrons, including the density gradient and collisions, is

$$\frac{d(m_e n_e \vec{v})}{dt} = en_e\left(\vec{E} + \vec{v} \times \vec{B}\right) - \nabla\left(n_e k T_e\right) - n_e m_e \vec{v}\nu_m \tag{11}$$

where $\vec{v}$ is the electron velocity and ν_m is the electron momentum transfer collision frequency. Eqs. (10) and (11) can be solved for $\overline{\overline{\mu}}(T_e)$ and $\overline{\overline{D}}(T_e)$, which describe the plasma flux vector field throughout the thruster, $\vec{\phi}$, according to the $\vec{E}$ and $\vec{B}$ fields. Obtaining an IV trace from he magnet ring electrodes is in general more desirable to inserting a Langmuir probe into the magnetic cusp, which would otherwise perturb current flow and lead to erroneous interpretation.

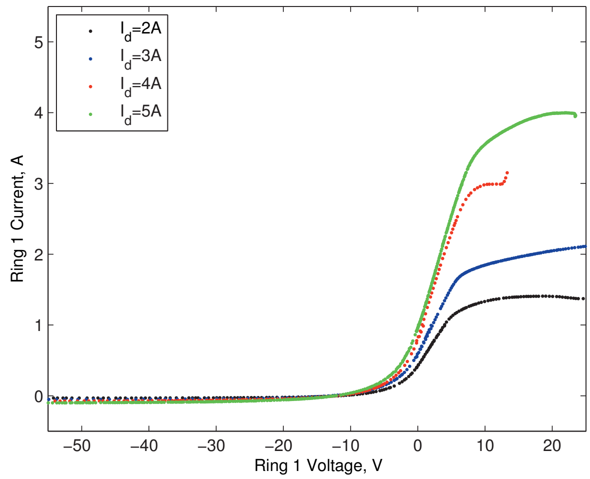

(a) Magnet ring electrode 1 current.

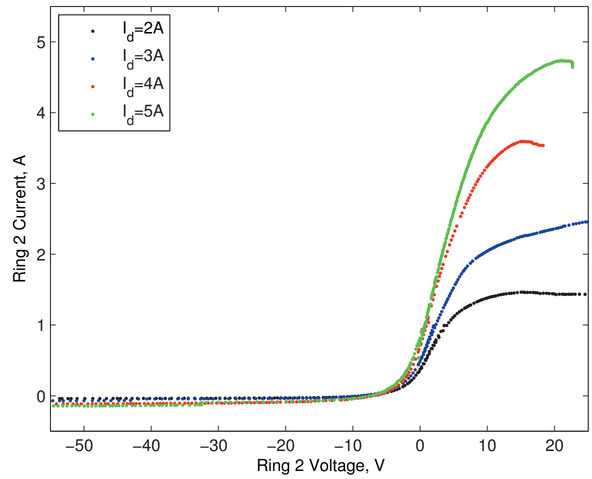

(b) Magnet ring electrode 2 current.

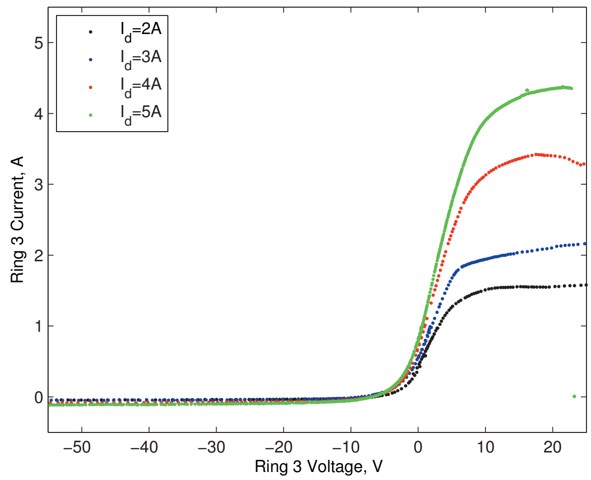

(c) Magnet ring electrode 3 current.

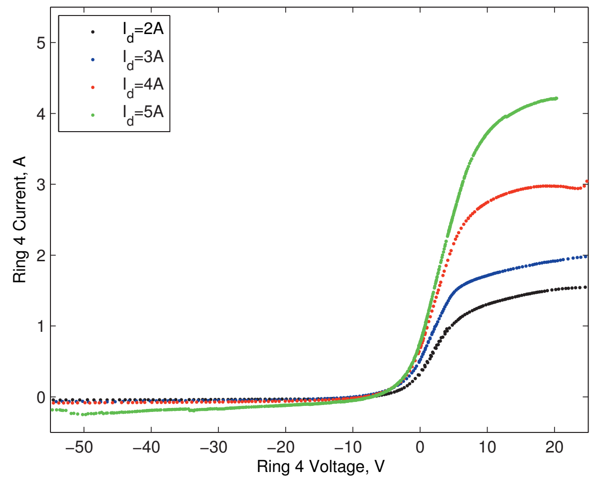

(d) Magnet ring electrode 4 current.

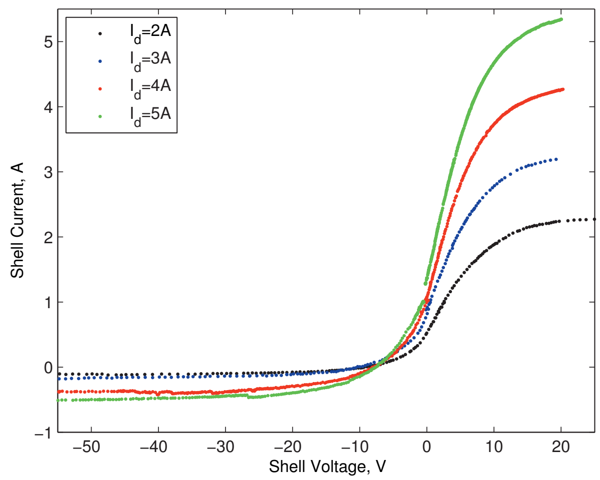

(e) Shell current.

Figure 8: Measured magnet ring electrode current as a function of bias voltage.

V. Analysis

The IV traces created by sweeping the magnet ring voltage can be analyzed using Langmuir probe theory. The ion saturation current, I_{si}, ion density, n_i, effective electron temperature, and saturation potential, V_{sat}, in the magnetic cusp are shown in Table 1. In the case of the bulk plasma measurements, V_{sat} is the plasma potential measured by the Mach probes. To calculate the ion density, an effective collection area for ions at the magnet rings must be calculated. This effective area depends on the leak width of the plasma through the cusp. The leak width at the magnetic cusp has previously been estimated as four times the hybrid Larmor radius:[12]

$$l_w = 4\sqrt{r_{li} r_{le}} \tag{12}$$

where r_{li} and r_{le} are the Larmor radii for ions and electrons respectively. The quantity $\sqrt{r_{li} r_{le}}$ is known as the hybrid Larmor radius. The Larmor radii are give by

$$r_{le,li} = \frac{v_\perp m_{e,i}}{e\mathbf{B}} \tag{13}$$

where $v_\perp$ is the particle velocity perpendicular to the magnetic field, $\vec{B}$. Multiplying Eq. (12) by the length of the magnet ring electrode gives the effective collection area for each ring electrode

$$A_{eff} = l_w \left(2\pi r_{mre}\right) \tag{14}$$

where r_{mre} is the radius of the magnet ring electrode. However, deep in the ion saturation region, no electrons are collected at the electrode, so the leak width is assumed to be only dependent on the ion Larmor radius; therefore the hybrid Larmor radius is replaced with the ion Larmor radius in Eq. (12). The leak width in Eq. (14) is replaced with the ion leak width,

$$l_{w,i} = 4r_{li} \tag{15}$$

In order to understand how the leak width changes as a function of electrode voltage, a non-intrusive diagnostic technique, such as LCIF, needs to be utilized.

Table 1: Plasma parameters from the magnet ring electrode traces at various discharge currents.

$I_d = 2A$					$I_d = 3A$				
	$I_{si}(A)$	$n_i(cm^{-3})$	$T_e(eV)$	$V_{sat}(V)$		$I_{si}(A)$	$n_i(cm^{-3})$	$T_e(eV)$	$V_{sat}(V)$
Ring 1	0.032	3.93×10^{10}	3.65	1.78	Ring 1	0.051	4.23×10^{10}	6.10	-0.46
Ring 2	0.040	2.07×10^{11}	3.38	2.03	Ring 2	0.071	3.16×10^{11}	4.37	3.14
Ring 3	0.046	2.56×10^{11}	3.02	1.76	Ring 3	0.052	2.52×10^{11}	3.29	1.98
Ring 4	0.044	2.41×10^{11}	4.15	2.65	Ring 4	0.075	2.87×10^{11}	3.81	1.91
Shell	0.122	4.94×10^{9}	5.39	3.25	Shell	0.181	6.96×10^{9}	4.71	2.64
Bulk		1.09×10^{12}	5.84	13.25	Bulk		1.47×10^{12}	6.07	14.31
$I_d = 4A$					$I_d = 5A$				
	$I_{si}(A)$	$n_i(cm^{-3})$	$T_e(eV)$	$V_{sat}(V)$		$I_{si}(A)$	$n_i(cm^{-3})$	$T_e(eV)$	$V_{sat}(V)$
Ring 1	0.075	8.51×10^{10}	3.74	2.39	Ring 1	0.101	1.26×10^{11}	4.84	3.14
Ring 2	0.116	6.36×10^{11}	4.20	3.43	Ring 2	0.145	6.61×10^{11}	7.38	1.11
Ring 3	0.086	4.84×10^{11}	3.62	2.96	Ring 3	0.117	5.80×10^{11}	3.41	2.98
Ring 4	0.087	4.21×10^{11}	3.66	2.56	Ring 4	0.249	8.42×10^{11}	4.04	3.44
Shell	0.423	1.80×10^{9}	5.16	2.47	Shell	0.513	2.27×10^{10}	5.01	2.41
Bulk		2.92×10^{12}	6.97	15.16	Bulk		2.56×10^{12}	7.02	14.45

The ring IV characteristics can be analyzed with simple Langmuir probe theory to obtain insight into the nature of particle collection. This approach can be applied to the ion saturation region since the ions are not appreciably magnetized and the electron retarding region since the magnetic field does not do work on the electrons. The macroscopic flux, ϕ, depends on the effective temperature according to the equation

$$\phi = \frac{1}{4} n_e \sqrt{\frac{8kT_e}{\pi m_e}} \tag{16}$$

The current collected at each ring electrode is dependent on this flux such that

$$I = \phi e A_{eff} \tag{17}$$

where A_{eff} is described by Eq. (14).

The data suggests the plasma density in the bulk differs depending on location (magnet ring number). The data also indicates that ion losses to the cusps rise with the discharge current. The V_{sat} from the ring electrode IV traces is lower than the bulk plasma potential. A schematic of the plasma potential profile at the bulk plasma to cusp interface is shown in Fig. 9.[8] This is in the case that the magnet ring electrode has no bias and is at anode potential. The potential in the cusp is expected to be less than the bulk plasma potential.[8]

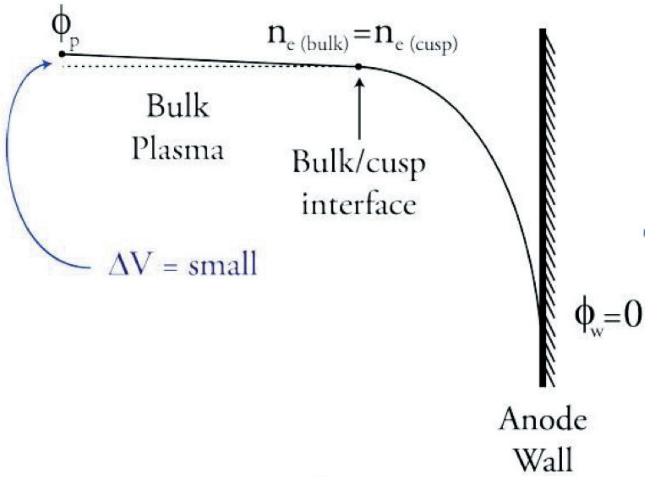

Figure 9: Schematic showing the plasma potential decreasing in the magnetic cusp.

The temperatures inferred from the rings are lower than the bulk electron temperature. This finding suggests that electrons that make it to the cusp region have cooled, presumably due to scattering collisions.

A. Mach Probe Measurements

The goal of this effort is essentially to modify the bulk plasma potential via biasing the cusp plasma. It was found that the largest changes in bulk plasma potential was realized when ring 3 was biased. This effort therefore focused on this magnet ring. Plasma parameters were measured using two Mach Probes in the bulk plasma. Fig. 10 shows the results of the Mach probe measurements when the bias on magnet ring electrode 3 is increased from 0 V to 25 V. Figure 10d illustrates bulk plasma potential changes with ring 3 bias voltage. As can be seen in the figure, a significant increase in plasma potential just upstream of the grid can be observed. Presumably, by biasing the ring at this voltage the actual plasma volume moves toward ring 3, as most of the discharge current is collected there under these conditions. A line depicting the estimated plasma potential profile is drawn in Fig. 10d. This line is based on the four points where the plasma potential was measured; each side of the two Mach probes. The lines in Fig. 10d are a conceptualization of the potential that the ions see within the discharge chamber. The grid has been biased to 30 V below cathode potential, so when the plasma potential is increased in the bulk, the ions see a larger potential decrease between the bulk plasma and the grid plane. Therefore the injection energy of the ions as they enter the grid sheath is increased, and their flow velocity is increased, as indicated by Fig. 10c. It should also be noted that the ion density, n_i, is increased by 11.1% and T_e increases by 0.7 eV. These increases are small and close to the error in the measurement. In summary, ring bias does appear to influence bulk plasma potential, thereby providing a means to enhance the ion drift field towards the grid.

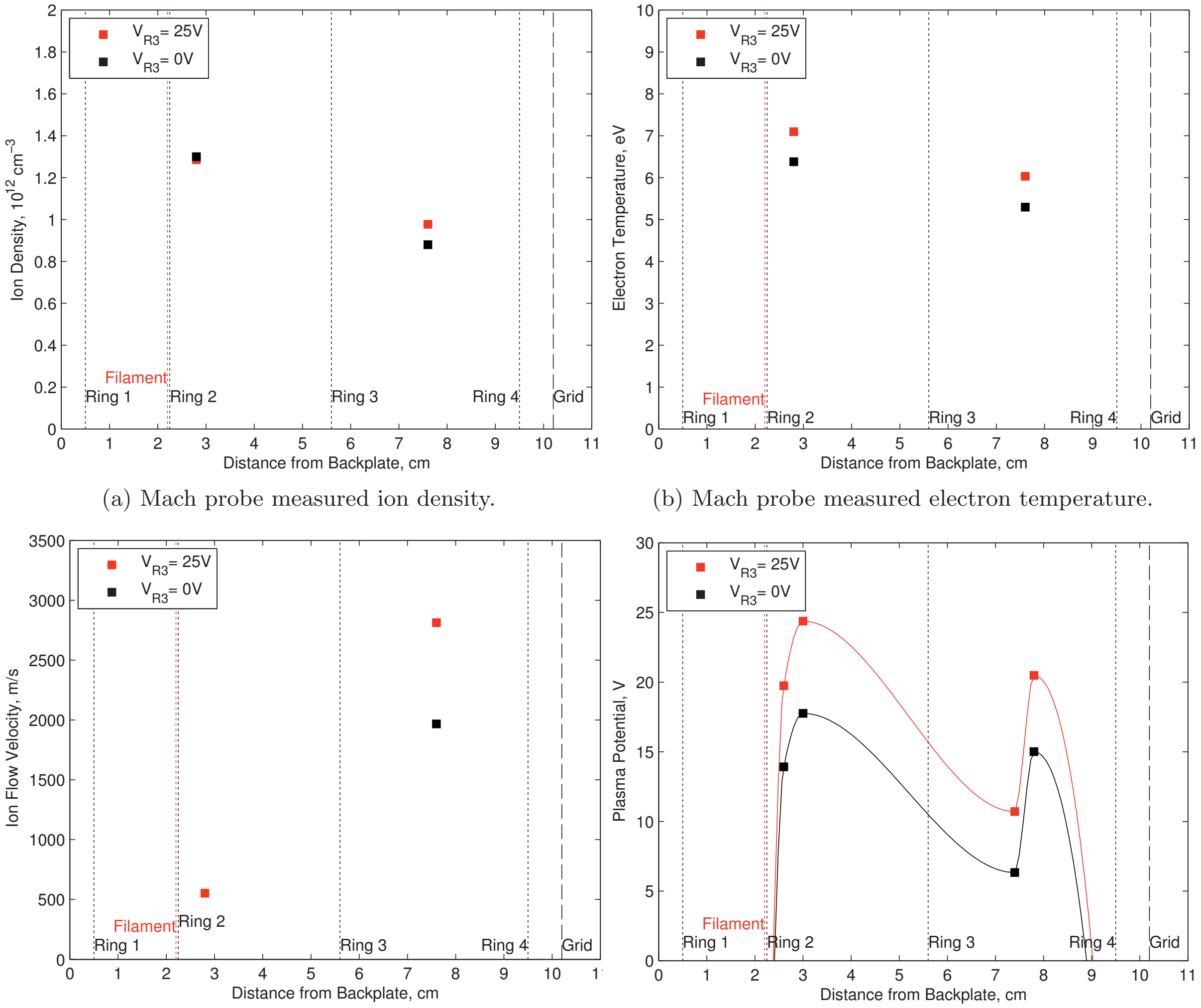

(a) Mach probe measured ion density.

(b) Mach probe measured electron temperature.

(c) Ion flow velocity as measured by both Mach probes.

(d) Estimated plasma potential profile.

Figure 10: Mach probe measured quantities while biasing magnet ring electrode 3 for a discharge current of 2A.

B. Grid Current Response

The grid current as a function of grid bias is shown in Fig. 11. The graph has a knee at 9.12 V, indicating that the grid voltage should be much greater than 9.12 V negative of cathode potential. This plot verifies the use of 30 V as the grid bias for the majority of the data presented.

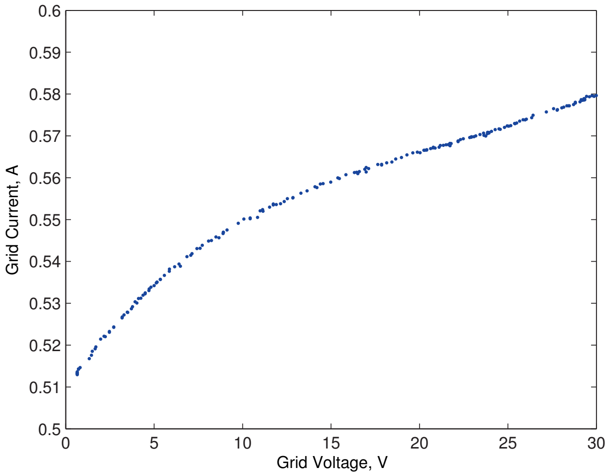

Figure 11: The collected grid current during simulated beam extraction as a function of grid bias voltage.

Of particular interest was how the collected grid current responds to the ring electrode bias voltage. Figure 12a illustrates the grid current response as the voltage on magnet ring 3 is increased. Indeed, biasing magnet ring electrode 3 positive of anode potential increased the ion current to the grid. Increasing grid current with increasing magnet ring bias agrees with qualitative Mach probe measurements and the inferred changes in the ion drift electric field derived from the plasma potential measurements. The saturation behavior is most likely due to saturation in electron current to the magnet ring. Once this occurs, the loss rate at the cusp is maximized—equaling the arrival rate at the cusp. Plasma potential no longer will change with increases in the bias voltage since the loss rate is no longer changing. Increased grid current without beam extraction could translate into increased beam current when a true set of ion optics is used with an actual engine.

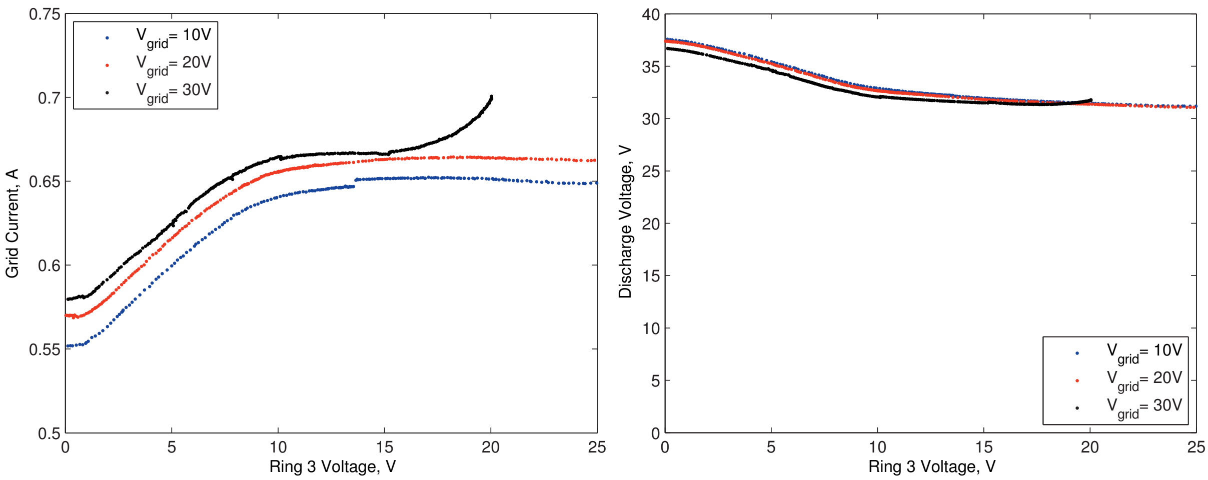

(a)

(b)

Figure 12: The (a) collector grid current and (b) discharge voltage as a function of magnet ring electrode 3 voltage.

In the case where the grid is biased to 30 V below cathode potential, the grid current begins to take off for high magnet ring 3 voltages. The discharge voltage for each case is also plotted in Fig. 12b to try to understand this take off in grid current. The discharge voltage does not fluctuate much as the grid current takes off as compared to the discharge voltage for other grid bias voltages. The behavior may be due to ionization within the grid sheath itself.

C. Electrode Collection Area

The determination of trends in local plasma properties inferred from the ring IV characteristic used an estimate of the effective loss area. This estimate is based on past studies of magnetic cusp collection.[8,12] The effective collection area of the magnetic cusp can also be deduced from the magnet ring electrode IV traces, Fig. 8. The electron saturation current collected at each electrode is given by

$$I_{sat} = en_e A_{eff} \sqrt{\frac{kT_e}{2\pi m_e}} \tag{18}$$

This effective area, A_{eff}, that is measured using Eq. (18) is compared to the the A_{eff} from Eq. (14), which is based on the hybrid Larmor radius over voltages that constitute the retarding region. The measured A_{eff} is plotted in Fig. 13, where the the solid red line is the A_{eff} based on the hybrid Larmor radius. Here it is assumed that the electron temperature does not vary appreciably. The values used to calculate the hybrid Larmor radius are taken from the Mach probe measurements in the bulk plasma. As can be seen in Fig. 13 the effective loss area does appear to approach the hybrid leak area with increasing voltage. Here the collector electrode is below plasma potential, so hybrid radius scaling is expected.

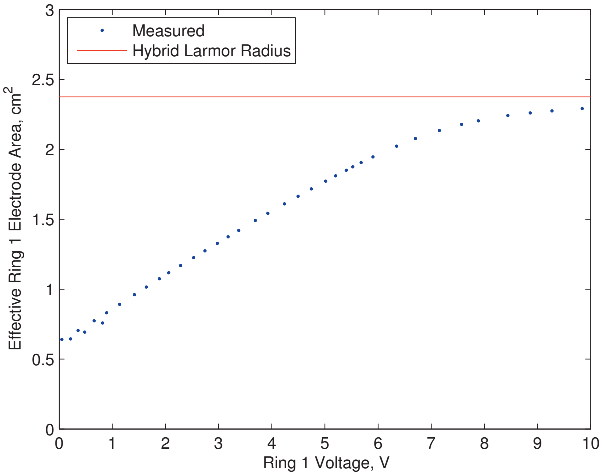

Figure 13: The measured current collection area of magnet ring electrode 1 as a function of voltage.

The effective collection area of the shell is shown in Fig. 14. A_{eff} for the shell is about a factor of 1000x times less than the physical area of the shell, which is shown as the solid red line. This is expected because the inter-cusp magnetic field contains electrons in the bulk plasma and prevents electrons from streaming to the walls. The effective shell collection area in Fig. 14 can be compared to the Hall parameter, β, which relates the electron cyclotron frequency to the electron momentum transfer collision frequency.

$$\beta = \frac{\Omega_e}{\nu_m} \tag{19}$$

where the electron cyclotron frequency, Ω_e, is given by

$$\Omega_e = \frac{e\mathbf{B}}{m_e} \tag{20}$$

The momentum transfer collision frequency, ν_m, is given by

$$\nu_m = N_g \sigma_m \sqrt{\frac{8kT_e}{\pi m_e}} \tag{21}$$

where N_g is the neutral gas density and σ_m is the momentum transfer cross section. The classical reduction in effective shell area is dependent on β according to the equation

$$\frac{A_{eff}}{A_{act}} = \frac{1}{1+\beta^2} \tag{22}$$

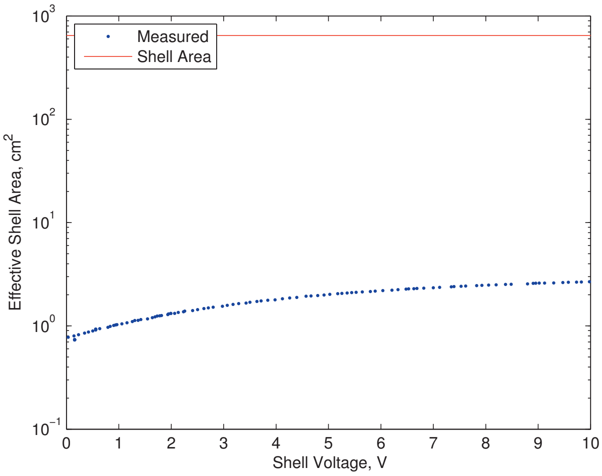

Figure 14: The measured current collection area of the shell as a function of voltage.

The reduction in effective shell area as measured is about 1.2×10^{-3}. This represents an average value, as in reality the inter cusp magnetic field varies spatially between magnetic cusps. As the magnetic field varies from 20 G in the bulk to 200G near the shell (between magnet rings), the effective area is reduced by a factor of 2.13×10^{-4} to 2.13×10^{-6}. The fact that the measured reduction in effective shell area is larger than the calculated value suggests that the electron diffusion across field lines is not completely classical. There is also uncertainty in the magnitude of the $\vec{B}$-field at the point that the electrons undergo collisions. The neutral gas temperature within the thruster is uncertain as well, which, along with the background pressure in the chamber, determines the neutral gas density.

D. RPA Measurements

In order to verify that biasing a magnet ring electrode was affecting the ion injection energy into the grid plane. The ion energy distribution function (IEDF) was measured using a retarding potential analyzer (RPA). The ion current measured at the RPA collector, I_C, was fit to a curve with the form[13]

$$I_C(V_D) = eA_{RPA}n_i(OAF)\left\{\frac{v_i}{2}\left[1 + erf\left(\sqrt{\frac{M_i}{2kT_i}}\left(v_i - \sqrt{\frac{2e\left(V_D - V_p\right)}{M_i}}\right)\right)\right]\right.$$
$$\left. + \sqrt{\frac{kT_i}{2\pi M_i}} exp\left[-\left(\sqrt{\frac{M_i}{2kT_i}}\left(v_i - \sqrt{\frac{2e\left(V_D - V_p\right)}{M_i}}\right)^2\right)\right]\right\} \quad (23)$$

where V_D is the RPA discriminator voltage and V_p is the plasma potential. The curve fit in Eq. (23) is used to reduce the measurement noise produced when taking the derivative of the RPA collector current. The derivative of the RPA collector current is proportional to the IEDF, such that[13]

$$f(V_D)_{Exp.} = -\frac{M_i}{2e^2A_{RPA}n_i(OAF)}\frac{dI_C(V_D)}{dV} \quad (24)$$

where A_{RPA} is the surface area of the RPA entrance. The derivative of the curve fit can be compared to a drifting Maxwellian fit, according to the equation[13]

$$f(V_D)_{Max.} = \sqrt{\frac{M_i}{2\pi kT_i}} exp\left[-\frac{M_i}{2\pi kT_i}\left(\sqrt{\frac{2e\left(V_D - V_p\right)}{M_i}} - v_i\right)^2\right] \quad (25)$$

The measured RPA collector current as a function of discriminator voltage is shown in Fig. 15 as well as the curve fit from Eq. (23). The curves in Fig. 15c clearly show that increasing the bias voltage of magnet ring electrode 3 causes a shift in the measured RPA collector current. The derivative of the curves in Fig. 15c is compared to the drifting Maxwellian fit of Eq. (25) and is shown in Figs. 16a and 16b. These figures show that the IEDF is close to a drifting Maxwellian, and in the case where magnet ring electrode 3 is biased to 10 V, the IEDF is estimated extremely well by a drifting Maxwellian. A comparison of the IEDFs produced when the ring electrode voltage is increased from 0 V to 10 V is shown in Fig. 16c. The IEDF peak is shifted from 6.39 eV to 7.44 eV. The average energy of the IEDF increases from 9.00 eV to 10.49 eV when magnet ring electrode 3 is biased to 10 V. The average energy is increased by a larger amount than the peak because the tail of distribution is more populated when the electrode is biased. The RPA data does not reflect the expected 5 V increases in ion energy inferred from changes in the plasma potential. This is probably due to the ions being slowed down by charge exchange collisions in the chamber. The background pressure in the chamber was 7×10^{-4} Torr. The mean free path for argon charge-exchange collisions at this pressure was calculated to be about 10 cm. Locally the pressure is higher at the source so that beam degradation may have been significant. The RPA had to be placed roughly a mean free path away from the grid plane to reduce plasma flow into the RPA. The placement of the RPA most likely influenced the measured IEDF and reduced the measured ion energy shift by a factor that is on the order of e^{-1}. The shift in the IEDF as measured by the RPA verifies that the ion injection energy into the grid is increased when the magnet ring electrode is biased.[14] This data reinforces the ion drift velocity measurements made by the Mach probe and presented in Fig. 10c.

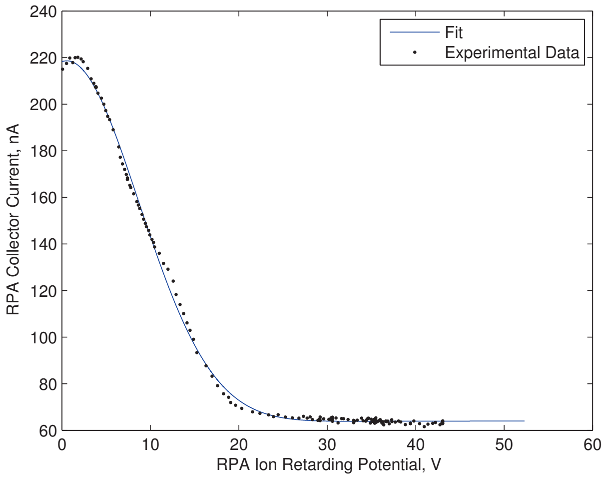

(a) Measured RPA collector current for V_{R3}=0V.

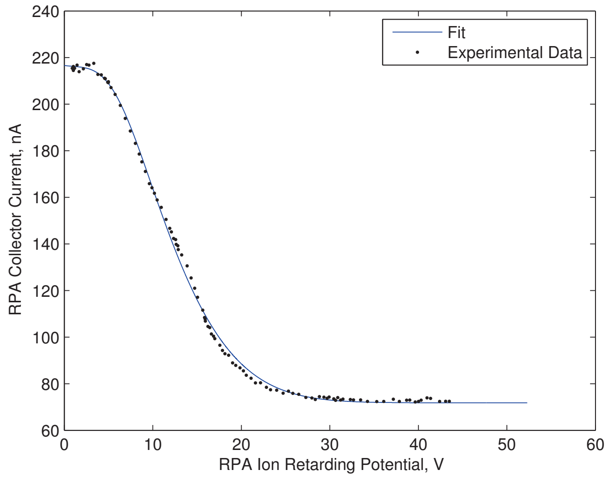

(b) Measured RPA collector current for V_{R3}=10V.

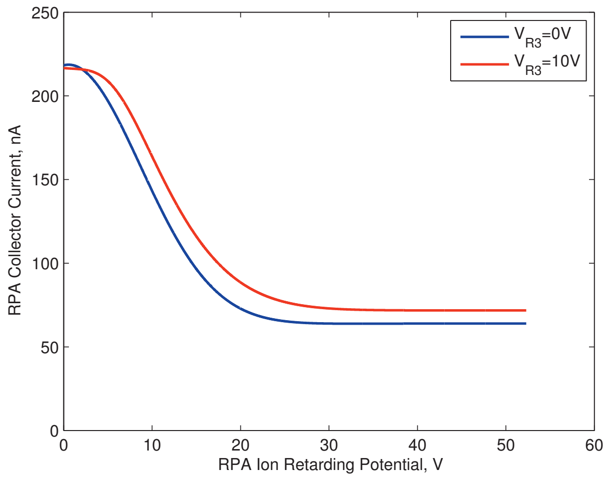

(c) Comparison of the fitted RPA data showing the shift produced by biasing magnet ring electrode 3.

Figure 15: Measured RPA collector current with curve fits according to Eq. (23).

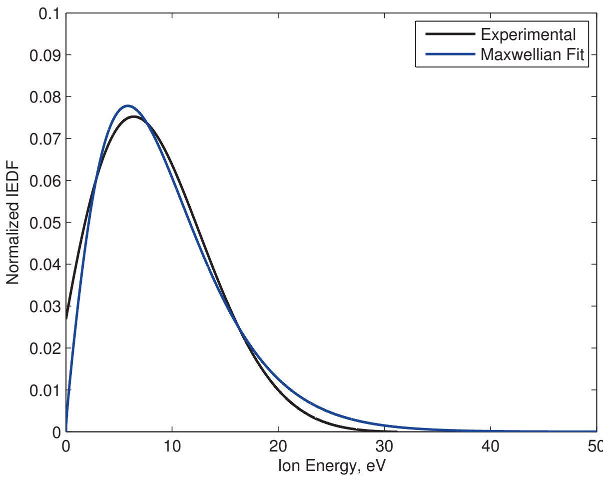

(a) RPA IEDF for V_{R3}=0V.

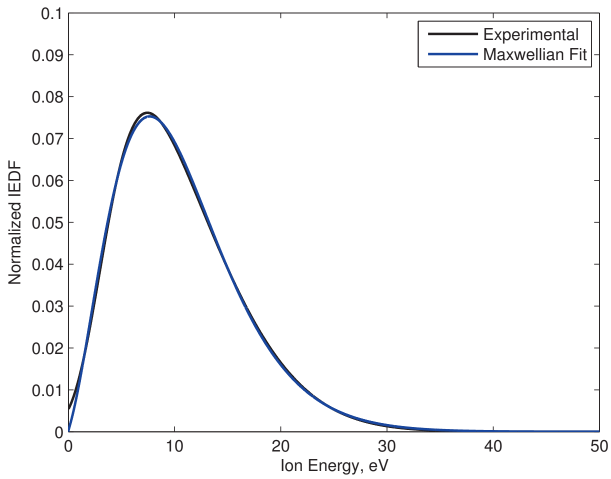

(b) RPA IEDF for V_{R3}=10V.

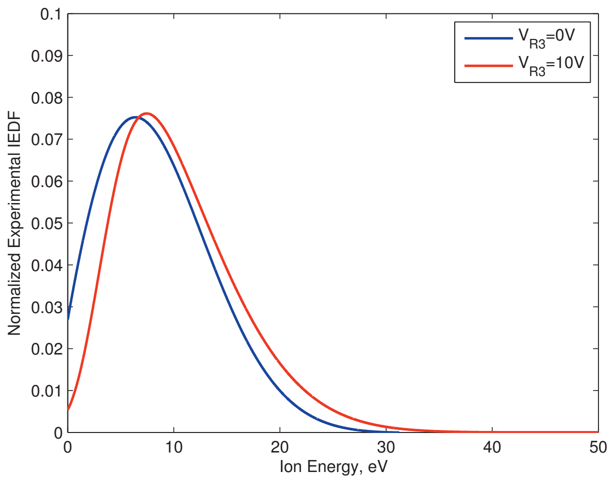

(c) Comparison of the experimental RPA IEDF showing the shift produced by biasing magnet ring electrode 3.

Figure 16: RPA IEDF curves for two different magnet ring electrode 3 bias voltages.

VI. Conclusion

The extractable beam current in an ion thruster is limited by the Child-Langmuir law. This work investigates an approach to increasing ion drift such that ion flux to the grids is increased and the true space charge limit is extended to higher currents at a given total voltage. Magnetic cusp biasing was used to affect bulk plasma potential and thus increase the ion drift field in the source. Enhanced drift was verified using three diagnostics: 1) Mach probe, 2) an RPA, and 3) a collector grid.

The measured current as a function of magnet ring electrode bias voltage produced IV characteristics which were analyzed using Langmuir probe theory. These calculations describe the plasma transport through the magnetic cusps. The measured ion saturation current describes the ion density in the cusp region and the measured effective electron temperature describes the macroscopic electron flux through the cusp.

Future work includes investigating the plasma properties in the cusp as the ring electrode is biased. This would be accomplished through the use of a non-intrusive diagnostic, such as LCIF. Detailed RPA measurements will be required to better assess the induced ion drift. The question of what happens to the plasma spatial distribution when rings are strongly biased is an open question. Spatial maps of electron density within the source as a function of bias voltage will also be carried out in future work.

Acknowledgments

The authors would like to acknowledge the University of Michigan Energy Institute and Michigan Phoenix Memorial Project for supporting the research presented in this paper.

References

[1] Patterson, M. J. and Foster, J. E.,"Performance and optimization of a derated ion thruster for auxiliary propulssion," *Joint Propulsion Conference*, AIAA Paper 91-2350, NASA, 1991.

[2] Soulas, G. C., Haag, T. W., and Patterson, M. J.,"Performance Evaluation of 40 cm ion optics for the NEXT ion engine," *Joint Propulsion Conference*, AIAA Paper 2002-3834, 2002.

[3] Patterson, M. J., Foster, J. E., Young, J. A., and Crofton, M. W.,"Annular Engine Development Status," *Joint Propulsion Conference*, AIAA Paper 3892, 2013.

[4] Patterson, M. J. and Rawlin, V. K., "Performance of 10-kW Class Xenon Ion Thrusters," *Joint Propulsion Conference*, AIAA Paper 88-2914, 1988.

[5] Goede, A. P. H. and Green, T. S., "Operation limits of multipole ion sources," *Phys. Fluids*, Vol. 25, No. 1797, 1982, pp. 1797-1810.

[6] Puri, R. R., Biswas, D. and Kumar, R., "Generalization of the Child-Langmuir law for nonzero injection velocities in a planer diode," *Physics of Plasmas*, Vol. 11, No. 3, 2004, pp. 1178-1186.

[7] Hubble, A. A, Foster, J. E., Barnat, E. V., and Weatherford, B. R., "Laser-Collisional Induced Fluorescence Study of Electron Distributions in a Magnetic Cusp," *International Electric Propulsion Conference*, IEPC-2013-367, 2013.

[8] Hubble, A. A., "Experimental Assessment of Plasma Transport in Magnetic Multicusp Ion Sources," Ph.D. Dissertation, Nuclear Engineering and Radiological Sciences Dept., The Univ. of Michigan, Ann Arbor, MI, 2013.

[9] Hutchinson, I. H.. "Ion collection by a sphere in a flowing plasma: I. Quasineutral," *Plasma Physics and Controlled Fusion*, Vol. 44, No. 9, 2002, pp. 1953-1977.

[10] Kardon, B. M., "Measurement of Plasma Flows using Mach Probe Arrays," Dissertation, Physics Dept., Massachusetts Inst. of Technology, Cambridge, MA, 2008.

[11] Brophy, J. R., "Simulated ion thruster operation without beam extraction," *International Electric Propulsion Conference*, AIAA Paper 90-2655, NASA, 1990.

[12] Hershkowitz, N., Leung, K. N., and Romesser, T., "Plasma leakage through a low-β line cusp." *Physical Review Letters*, Vol. 35, No. 5, 1975, pp. 277-280.

[13] Fang, H. K. and Cheng, C. Z., "Retarding Potential Analyzer (RPA) for Sounding Rocket," *An Introduction to Space Instrumentation*, TerraPub, Tokyo, Japan, 2013, pp. 139-153.

[14] Foster, J. E. and Patterson, M. J., "Internal Plasma Properties and Enhanced Performance of 8-Centimeter Ion Thruster Discharge," *Journal of Propulsion and Power*, Vol. 17, No. 2, 2001, pp. 428-432.

[15] Hanson, W. B., Santani, S., Zuccaro, D., and Flowerday, T. W., "Plasma Measurements with the Retarding Potential Analyzer on Ogo 6", *Journal of Geophysical Research*, Vol. 75, No. 28, 1970, pp. 5483-5501.

[16] Goebel, D. M., "Ion source discharge performance and stability." *Physics of Fluids*, Vol. 25, No. 6, 1982, pp. 1093-1102.

[17] Goebel, D. M., Jameson, K. K., Katz, I., and Mikellides, I. G., "Potential fluctuations and energetic ion production in hollow cathode discharges," *Physics of Plasmas*, Vol. 14, No. 10, 2007, 103508.

[18] Kaufman, H. R. and Robinson, R. S., *Operation of Broad-Beam Sources*, Commonwealth Scientific Corporation, Alexandria, VA, 1987.